Arabian Journal of Chemistry (2023) **16**, 104749

King Saud University

Arabian Journal of Chemistry

www.ksu.edu.sa
www.sciencedirect.com

ORIGINAL ARTICLE

Efficient photocatalysis of Cu doped TiO_2/g-C_3N_4 for the photodegradation of methylene blue

Heshan Liyanaarachchi [a], **Charitha Thambiliyagodage** [a,*], **Chamika Liyanaarachchi** [a], **Upeka Samarakoon** [b]

[a] *Faculty of Humanities and Sciences, Sri Lanka Institute of Information Technology, New Kandy Road, Malabe, Sri Lanka*
[b] *Department of Nano Science Technology, Faculty of Technology, Wayamba University of Sri Lanka, Kuliyapitiya, Sri Lanka*

Received 30 October 2022; accepted 23 February 2023
Available online 6 March 2023

KEYWORDS

Cu doped TiO_2;
g-C_3N_4;
Methylene blue;
Photodegradation;
UV;
Visible

Abstract The release of dyes into normal water reservoirs has become a tremendous environmental problem and the development of methods to remove such dyes is essential. A novel photocatalyst was fabricated in which Cu doped to TiO_2 was coupled with g-C_3N_4 (Cu-TiO_2/g-C_3N_4) in different weight percentages as 10, 30 and 50%, hydrothermally. Pure TiO_2 consisted of both Anatase and Rutile phases where slight lattice distortions were observed in the Cu-doped TiO_2 as evidenced by the XRD and Raman analysis. Cu was present at 1.7% by weight respective to TiO_2 according to the XRF analysis. Spherical and irregularly shaped aggregated Cu-doped TiO_2 nanoparticles in the range of 15–55 nm were heterogeneously distributed on the g-C_3N_4 matrix as observed by TEM and SEM. The band gap of TiO_2 (3.0 eV) was reduced to 2.67 upon doping with Cu. The band gap of g-C_3N_4 was found to be 2.81 eV and that of Cu-TiO_2/g-C_3N_4 in different weight percentages were in the range of 2.82 to 2.88 eV. Synthesized photocatalysts were tested on the ability to degrade methylene blue under UV and Visible light. Cu-TiO_2/50% g-C_3N_4 showed the highest rate constant (4.4×10^{-3} min^{-1}) which is 5 and 9.8 times greater than TiO_2 and g-C_3N_4, respectively. The rate constant decreased with the introduction of EDTA and Isopropyl alcohol as they scavenge holes and hydroxyl radicals, respectively. The photocatalytic activity of all the nanomaterials increased with the increasing concentration of persulfate due to the increasing concentration of $SO_4^{\bullet-}$ and $OH^{\bullet}$ produced. Synthesized nanomaterials effectively adsorb methylene blue under dark conditions following the pseudo-second-order kinetics suggesting that methylene blue molecules were chemisorbed to the adsorbents. The adsorption rate constant resulting in the

* Corresponding author.
E-mail address: charitha.t@sliit.lk (C. Thambiliyagodage).
Peer review under responsibility of King Saud University.

Production and hosting by Elsevier

https://doi.org/10.1016/j.arabjc.2023.104749

best-performing photocatalyst was 0.122 g mg^{-1} min^{-1}. Hence, it is evident that Cu-TiO_2/g-C_3N_4 can effectively degrade methylene blue.

1. Introduction

Water pollution is a tremendous problem being emerged in the last few decades due to industrialization, urbanization and economic revolution. Organic pollutants including but not limited to dyes, pesticides, and pharmaceuticals are released to water reservoirs and cause severe hazardous effects because they persist in the environment as they are resistant to degradation. Therefore, water purification is eliciting attracting scientists to mitigate the severe effects resulting from the pollutants. Among the many organic pollutants that are being discharged into water, dyes which are released from textile, paper, paint (Al-Tohamy et al., 2022; Parmar et al., 2022; Silva et al., 2021) etc. industries play a major role as they are constituted of heavy metals (Singha et al., 2021) and aromatic compounds (Faria et al., 2008) in addition to the dye molecules. Dyes in aquatic environments cause health risks to living organisms, reduce the light penetration into the water body and hence reduce the photosynthetic efficiency of aquatic plants which also leads to producing anoxic conditions that impact the aquatic fauna and flora (Dutta & Bhattacharjee, 2022). They degrade the aesthetic value of the water bodies due to the persistent colours and increase the biological and chemical oxygen demand (Azanaw et al., 2022). Further, they get accumulated in the food chain and promote toxicity leading to many severe health conditions (Lellis et al., 2019). Therefore, it is vital to remove the dyes from normal water reservoirs. Many methods including membrane filtration (Ramutshatsha-Makhwedzha & Nomngongo, 2022), adsorption (Birniwa et al., 2022; Gunathilaka et al., 2021), ion exchange (Lu et al., 2022), coagulation (Ihaddaden et al., 2022), oxidation (Javanbakht & Mohammadian, 2021), hydrogenation catalysis (J. Thambiliyagodage et al., 2016) etc. have been employed to remove dyes from contaminated water. However, these methods possess different disadvantages such as sludge production, high cost, incomplete removal, poor mass transfer, low permeability, unsuitable for larger volumes, formation of toxic byproducts etc. despite their advantages of being effective in a wide range of dyes, eco-friendliness, effective decolourization etc (Moosavi et al., 2020). Hence, it is necessary to develop a new technique to alleviate the existing problem which could overcome the drawbacks shown by the established methods and be more advantageous including being efficient.

The advanced oxidation process (AOP) involves the generation of reactive oxygen species such as $OH^{\bullet}$, $O_2^{\bullet}$, H_2O_2, and O_3 which degrade the pollutant molecules into harmless products. Degradation of methylene blue by many AOP methods including ozonation (Babar et al., 2022), photocatalysis (Thambiliyagodage, Kumara, et al., 2022), Fenton (Kirchon et al., 2020), sonolysis (Bezzerrouk et al., 2021), and electrochemical oxidation (Samarghandi et al., 2020) have been reported. However, these methods possess disadvantages such as toxicity of by products, the requirement of large quantities of H_2O_2, effective in low pH, the requirement of sophisticated equipment, highly expensive etc. (X. Li et al., 2021; Lyu et al., 2016; Pirsaheb & Moradi, 2021). Photocatalysis is advantageous over the other methods because methylene blue is degraded into harmless products such as CO_2, H_2O, NH_4^+, SO_4^{2-} and NO_3^- (Charitha et al., 2021).

Semiconductors are employed in mineralizing organic molecules via AOP and the most widely used semiconductor is TiO_2 due to its stability, non-toxicity and low cost (Guo et al., 2019). However, TiO_2 bearing a band gap of 3.2 eV in general is active only in the UV range limiting its applicability in the visible range (Sharma et al., 2019). TiO_2 has been doped with metals like Fe (Thambiliyagodage & Mirihana, 2021), Cu (Lee et al., 2021), and Mn (Lee et al., 2021), and non-metals such as N (Thambiliyagodage & Usgodaarachchi, 2021), C (Pandi et al., 2022), and S (T. Li et al., 2021) to reduce the band gap to increase the visible light sensitivity. However, the photocatalytic activity is reduced due to the electron-hole pair recombination even though in general the photocatalytic activity in visible light is enhanced via reducing the band gap. Therefore, to enhance the charge separation TiO_2 has been coupled with other semiconductors forming type I and type II heterojunctions. Semiconductors including WO_3 (H. Li et al., 2021), Fe_2O_3 (Fawzi Suleiman Khasawneh & Palaniandy, 2021), BiOI (Liao et al., 2022), and MoS_2 (Y. Wu et al., 2022) form type I heterojunctions with TiO_2 while semiconductors like CuO (Shi et al., 2019), CdSe (M. Yang et al., 2018), V_2O_5 (Ghosh et al., 2018), CeO_2 (Tuyen et al., 2018), Bi_2S_3 (Z. Wu et al., 2020), WS_2 (Jing & Guo, 2007), Bi_2O_3 (Lakshmana Reddy et al., 2017) form type II heterojunctions.

g-C_3N_4 is a metal-free semiconductor which is normally synthesized by precursors such as urea, melamine, cyanamide etc. It is comprised of s-triazine or tri-s-triazine units as the structural monomers where the sheets resemble the structure of the honeycomb. Atoms of one sheet are interconnected via covalent bonds and the sheets are held together by Vander Waals forces (Yu et al., 2023). g-C_3N_4 has been coupled with other materials including TiO_2 (Kobkeatthawin et al., 2022), ZnO (Geng et al., 2021), Fe_2O_3 (Pham et al., 2022), SnO_2 (Van et al., 2022), V_2O_5 (Preeyanghaa et al., 2022), Bi_2O_4 (J. Yang et al., 2020), α-MoC1-x quantum dots (Zhu et al., 2022), charcoal (Yu et al., 2020) etc. and also with to maximize the charge separation as g-C_3N_4 is taken individually electron-hole pair recombination was found to be a problem which leads to lower photocatalytic activity.

According to our knowledge coupling of g-C_3N_4 with TiO_2 doped with metals has not been reported in detail. Metal-doped TiO_2 possess a reduced band gap being active in the visible range but shows low photocatalytic activity due to electron-hole pair recombination while as discussed above g-C_3N_4 also exhibits the same disadvantage. Therefore, coupling such two semiconductors would be advantageous as both the semiconductors are visible active. Hence, Cu doped TiO_2 was coupled with g-C_3N_4 to form a z-scheme heterojunction and the photocatalytic activity of the synthesized nanocomposite was evaluated in the photodegradation of methylene blue.

2. Materials and methods

2.1. Materials

P25 TiO_2 (99.5%) and Urea (99.5%) were purchased from Sigma Aldrich, German. $CuCl_2{\cdot}2H_2O$ (99%) was procured from Sisco Research Laboratories (Pvt) Ltd, India. Methylene blue (98%) was purchased from Himedia Laboratories (Pvt) Ltd, India. All the chemicals were used as it is without further purification. Distilled water was used for all the experiments.

2.2. Procedure

2.2.1. Synthesis of Cu-TiO_2

P25 TiO_2 was dispersed in distilled water. $CuCl_2{\cdot}2H_2O$ was dissolved in distilled water where the molar percentage of Cu was maintained at 1% with respect to Ti and the obtained solution was added dropwise to the solution containing P25 while stirring. Stirring continued for 24 h and the obtained pre-

cipitate was washed with distilled water until the filtrate was negative for Cl^- ions for the $AgNO_3$ test. Then the temperature was increased and maintained at 80 °C until all water evaporates. The resulting solid was ground and calcined at 450 °C for 2 h. The product is denoted as Cu-TiO_2 in the text.

2.2.2. Synthesis of g-C_3N_4

The urea was annealed in a tube furnace at 550 °C for 4 h under N_2 atmosphere and the resulting yellow colour product was washed with distilled water and ethanol, followed by drying at 80 °C.

2.2.3. Synthesis of Cu-TiO_2/C_3N_4

g-C_3N_4 was mixed with Cu-TiO_2 in different weight percentages as 10, 30 and 50 % and the product was sonicated for 1 h. The resulting mixture was hydrothermally treated at 180 °C for 15 h. The product obtained was washed with distilled water and ethanol and dried at 80 °C.

2.3. Characterization techniques

X-ray diffraction (XRD) patterns were collected using an Advance Bruker system using CuKα (λ = 0.154 nm) radiation and 2θ varying from 5°-80° at a scan speed of 2°/min. Raman spectra were acquired by a Bruker Senterra Raman microscope spectrometer. The morphology of the nanomaterials was observed by both scanning electron microscope (SEM) and transmission electron microscope (TEM). The transmission electron microscope was operated at 200 kV (JEOL - JEM – 2100). The sample (1 μl) was mounted on a holey carbon copper grid and allowed to dry at room temperature before TEM analysis. SEM images were collected by Hitachi SU6600 Analytical Variable Pressure FE-SEM (Field Emission Scanning Electron Microscope). Samples were mounted on a carbon tape pasted on a stub and the samples were sputtered with gold to neutralize the charge. The chemical composition of the samples was analyzed by X-ray fluorescence (XRF) using a HORIBA Scientific XGT-5200 X-ray analytical microscope equipped with a Rh anode X-ray tube operated at a maximum voltage of 50 kV. The surface chemistry of the nanomaterials was analyzed by X-ray photoelectron spectroscopy (XPS) using Thermo ScientificTM ESCALAB Xi + X-ray Photoelectron Spectrometer. Shimadzu 1800 UV/Visible spectrophotometer utilizing a precision Czerny-Turner optical system was used to analyze diffuse reflectance spectra of the prepared powder samples. The measurements were carried out through the range of 400 to 750 nm with a bandwidth of 1.0 nm (wavelength accuracy +- 0.1 nm). The absorbance of MB samples was measured by a Shimadzu UV-1990 double-beam UV–Visible spectrophotometer.

2.4. Photocatalysis

Each synthesized photocatalyst (200 mg) was shaken with 100 ml of 10 mg/L MB solution in dark for 1 h to reach the adsorption and desorption equilibrium during which aliquots were taken in different time intervals to study the adsorption kinetics. After that, the samples were exposed to a UV–Visible source operated with a 100 W mercury lamp (253 nm) and 100 W LED (589 nm) light and aliquots were withdrawn in 15 min time intervals to study the photocatalytic performance. To study the effect of scavengers EDTA (4 mM) and IPA (4 mM) were added just before exposing them to the light source. Similarly, to study the effect of persulfate on photocatalysis persulfate was added to the reaction mixture in different concentrations as 2, 4 and 8 mM and the photocatalysis experiments were carried out as described above.

3. Results and discussion

3.1. XRD analysis

XRD analysis was performed to determine the crystal structure of the synthesized nanomaterials. The XRD pattern of g-C_3N_4 shows two peaks at 13.00° and 27.04° which correspond to (100) and (002), respectively. XRD pattern of P25 TiO_2 shows peaks at 27.57°, 36.18°, 41.37°and 56.73° which are attributed to (110), (101), (111) and (220) planes of the Rutile phase and the peaks at 25.46°, 37.95°, 38.72°, 39.31°, 48.17°, 54.07°, 55.18°, 62.83°, 68.94°, 70.34° and 75.21° assigned to (101), (103), (004), (112), (002), (105), (211), (204), (115), (220) and (215) the Anatase phase (Fig. 1 (a)). The same peaks were observed in Cu-TiO_2 and Cu-TiO_2 composited with g-C_3N_4. The Interlayer distance (d) and the crystallite size (L) of the synthesized nanomaterial were calculated by equations 1 and 2, respectively, where,

λ - wavelength of the X-ray source
θ - diffraction angle
L - crystallite size
β - half maximum of the peak in radians
K - Scherer's constant (0.9)

$$\lambda = 2dsin(\theta). \quad (1)$$

$$L = K\lambda/\beta Cos\theta. \quad (2)$$

The interlayer distance and the crystallite size of g-C_3N_4 were 0.3293 nm and 2.591 nm and the number of planes in the synthesized g-C_3N_4 was 8. (101) plane of the Anatase phase and (110) of Rutile phase was considered for the calculation of the interlayer distance and crystallite size of those phases in P25 TiO_2 and they were calculated to be 0.3495 nm and 18.622 nm, respectively, for Anatase phase and 0.3232 nm and 29.263 nm, respectively, for Rutile phase. The number of planes in the Anatase phase is 53 and in the Rutile phase is 90.

Peaks corresponding to the same planes were considered for calculations of the same parameters in Cu-TiO_2 and Cu-TiO_2 composited with g-C_3N_4. Table 1summarizes all the data calculated relative to the crystalline structure of the synthesized nanomaterials. But peak positions of the (101) plane of Anatase and (110) plane of Rutile reduced in Cu doped sample than that of P25 suggesting the lattice distortion which may have occurred during doping of Cu (Fig. 1 (b)). No crystal peaks corresponding to Cu or oxide of Cu were observed suggesting that Cu has successfully doped to the P25 lattice. Generally, the crystallite size of the Anatase phase increased with the doping of Cu and compositing with g-C_3N_4. However, no such trend in crystallite size was observed with the Rutile

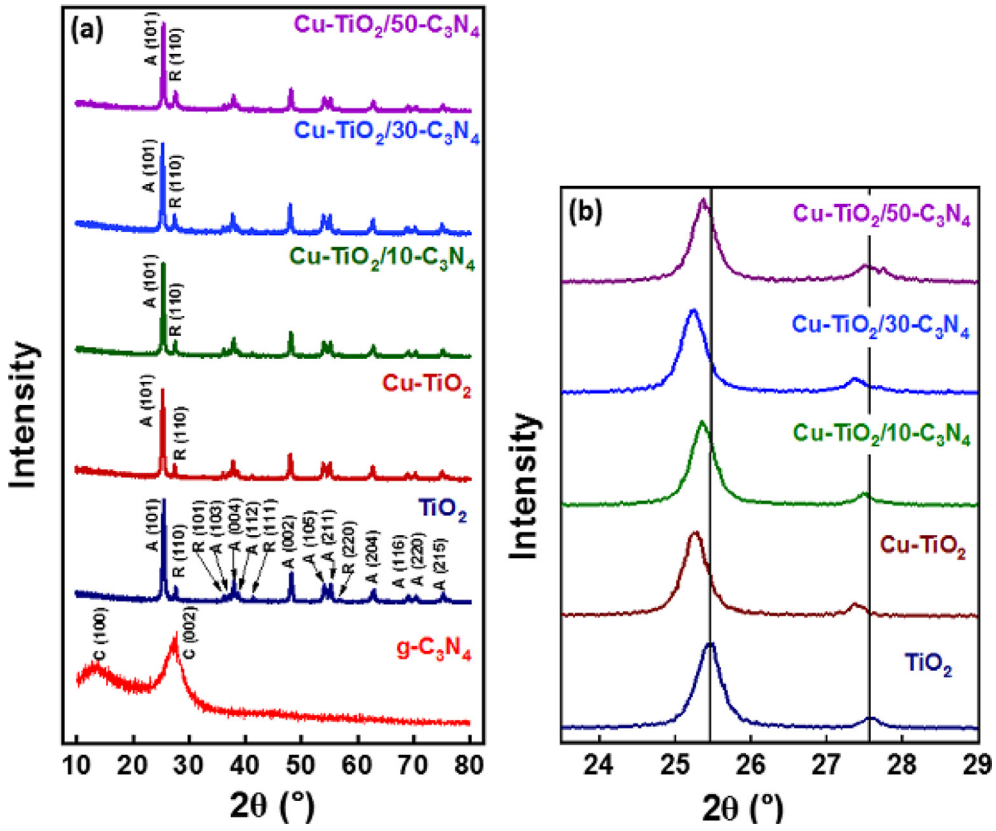

Fig. 1 (a) XRD pattern of the synthesized nanomaterials (b) partially enlarged XRD patterns between 24° and 29°.

Table 1 Crystallographic parameters of the synthesized nanomaterials.

Sample	Crystal Plane	2θ (°)	L (nm)	d (nm)	L/d
g-C_3N_4	C (002)	27.05	2.591	0.3293	8
TiO_2	A (101)	25.45	18.622	0.3495	53
	R (110)	27.57	29.263	0.3232	90
Cu-TiO_2	A (101)	25.26	18.995	0.3521	54
	R (110)	27.37	21.240	0.3254	65
Cu-TiO_2/10- C_3N_4	A (101)	25.36	19.317	0.3508	55
	R (110)	27.49	27.816	0.3240	85
Cu-TiO_2/30- C_3N_4	A (101)	25.24	18.996	0.3525	54
	R (110)	27.37	21.240	0.3255	65
Cu-TiO_2/50- C_3N_4	A (101)	25.36	19.456	0.3507	55
	R (110)	27.57	14.907	0.3232	46

phase. The interlayer distance of both Anatase and Rutile did not change upon doping with Cu or g-C_3N_4. This suggests that Cu^{2+} ions have been doped to the Anatase crystal structure of P25. The ionic radius of Cu^{2+} (73 pm) is quite similar to the ionic radius of Ti^{4+} (74 pm). Metal ions could be doped to TiO_2 interstitially or substitutionally and as the cationic radii of both are quite similar it is suggested that Cu^{2+} have replaced Ti^{4+} in the Anatase phase of TiO_2 lattice. Further, the absence of peaks attributed to Cu or oxide of Cu could be due to the good dispersion of those compounds if they have formed at the low concentration of Cu (1%) introduced during the synthesis.

3.2. Raman analysis

Raman analyses were performed to confirm the crystal structure suggested by XRD analysis (Fig. 2). The Raman spectrum of P25 TiO_2 shows peaks at 143 cm^{-1}, 196 cm^{-1}, 396.5 cm^{-1}, 515 cm^{-1} and 638.5 cm^{-1} which are attributed to E_g, E_g, B_{1g}, A_{1g} and E_g vibrational modes of Anatase phase (Balachandran & Eror, 1982; Hardcastle, 2011). Peaks relevant to the vibrational modes of the Rutile phase were absent. The Raman spectrum of Cu-TiO_2 is identical to that of P25. However, the peak corresponding to the E_g band appeared in P25 at 143 cm^{-1} while that in Cu-TiO_2 appeared at 144 cm^{-1} suggest-

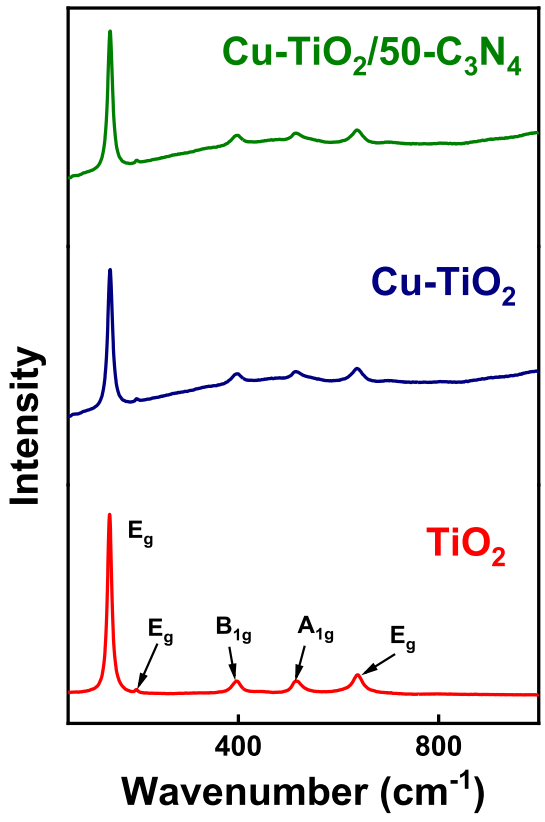

Fig. 2 Raman spectra of TiO_2, Cu-TiO_2 and Cu-TiO_2/50-C_3N_4.

ing a lattice distortion upon doping with Cu being consistent with the XRD analysis. The Raman spectrum of Cu-TiO_2/50-C_3N_4 is also identical to that of P25 and no peaks corresponding to g-C_3N_4 were observed.

3.3. TEM analysis

Transmission Electron Microscopy (TEM) is used to study the morphology of nanomaterials synthesized at the nanoscale. TEM image of g-C_3N_4 (Fig. 3 (a)) shows that thin and fluffy g-C_3N_4 nanosheets are arranged as tremella-like layers. Further, a mesoporous network has been formed in the nanosheets of g-C_3N_4 as revealed in Fig. 3 (b) due to the polymerization and the elimination of gas molecules during the annealing process. Nitrogen and oxygen in the reaction system can generate gas bubbles splitting the polymer when it polymerizes resulting in stripping g-C_3N_4 layers into small layers producing a fluffy structure. TEM image of P25 TiO_2 (Fig. 3 (c)) shows spherical homogeneously distributed nanoparticles along with some aggregated irregular shape particles. The crystalline plane arrangement of P25 TiO_2 is exhibited in the Higher resolution TEM (HRTEM) image (Fig. 3 (d)). Calculated interlayer distances, 0.23 nm and 0.35 nm correspond to the (1 0 3) plane and (1 0 1) plane of the Anatase phase, respectively. Cu-TiO_2 nanoparticles show spherical and irregular shape nanoparticles with some agglomerations (Fig. 3 (e)). HRTEM of Cu-TiO_2 (Fig. 3 (f)) clearly shows crystalline plane arrangements with interlayer distances of 0.35 nm and 0.32 nm, corresponding to the (1 1 0) plane of Anatase and (1 0 1) plane of the Rutile phase, respectively. TEM image of Cu-TiO_2/50-C_3N_4 (Fig. 3 (g)) shows spherical and aggregated nanoparticles heteroge-

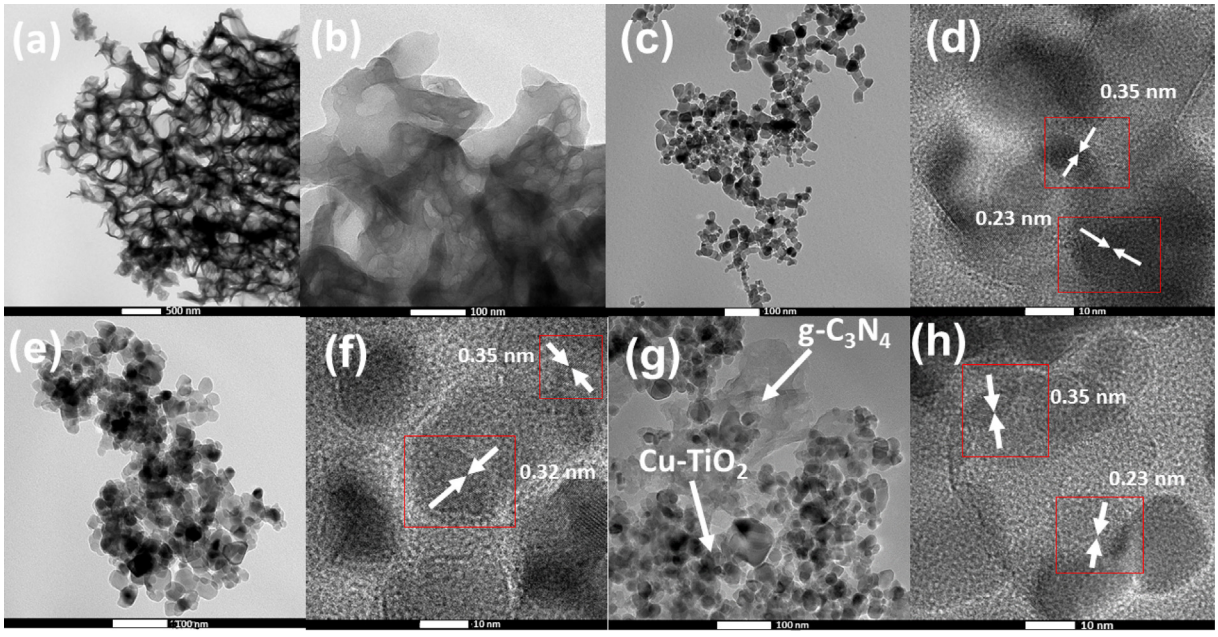

Fig. 3 TEM images of (a) g-C_3N_4 at low magnification (b) g-C_3N_4 at high magnification (c) P25 TiO_2 (d) HRTEM image of P25 TiO_2 (e) TEM image of Cu-TiO_2 (f) HRTEM image of Cu-TiO_2 (g) TEM image of Cu-TiO_2/50-C_3N_4 (h) HRTEM image of Cu-TiO_2/50-C_3N_4.

neously distributed on a fluffy nanosheet mesoporous network. HRTEM image of Cu-TiO_2/50-C_3N_4 (Fig. 3 (h)) shows the interlayer distances 0.35 nm and 0.23 nm corresponding to (1 0 1) and (1 0 3) planes of Anatase phase, respectively further supporting the crystal nature of the nanoparticles in the composite.

3.4. SEM analysis

SEM images were collected to study the morphology of the synthesized nanomaterials. SEM image of P25 TiO_2 (Fig. 4 (a)) shows the spherical and irregularly shaped nanoparticles with some agglomerations. Upon doping with Cu further agglomerations were observed which could have occurred during the synthesis and annealing (Fig. 4 (b)). SEM image of g-C_3N_4 (Fig. 4 (c)) exhibited a properly developed macropore structure where ligaments are interconnected to form a disordered macropore network and the insert of Fig. 4 (c) shows the irregularity of the macropores in high magnification. g-C_3N_4 possesses a well-established mesopore structure as shown in the TEM image (Fig. 3 (b)). These mesopores and macropores together form a hierarchical porous system where the two porous systems are interconnected forming channels for the reagents and products to pass through which is an important characteristic in catalysis. However, such porous structure has been disturbed upon coupling with Cu-TiO_2 as shown in Fig. 4 (d) in Cu-TiO_2/50-C_3N_4, as the nanoparticles which are high in weight proportion of the composite, mask and block the porous system. Further, Cu-TiO_2 nanoparticles are properly distributed on the g-C_3N_4 matrix which would facilitate the physical connection of the two materials, Cu-TiO_2 and g-C_3N_4, making them ideal candidates in catalysis.

Brunauer-Emmett-Teller (BET) surface area analysis was performed to study the surface area and the pore size distribution of the samples. Adsorption desorption isotherms and the pore size distribution curves of TiO_2, Cu-TiO_2, and Cu-TiO_2/50-C_3N_4 are shown in Supplementary Figure 1 (a) and (b), respectively. Isotherms exhibited type IV behaviour indicating the mesoporous structure. The surface area of Cu-TiO_2 (82.76 m^2/g) is lesser than that of TiO_2 (110.99 m^2/g) indicating the agglomeration resulted during doping while the surface area of Cu-TiO_2/50-C_3N_4 (35.46 m^2/g) is lesser than both. No significant change was found in the total pore volume of Cu-TiO_2 (0.38 cc/g) and TiO_2 (0.37 cc/g), and that of Cu-TiO_2/50-C_3N_4 (0.08 cc/g) was very low. The pore radius of Cu-TiO_2 (9.12 nm) is greater than that of TiO_2 (6.66 nm) indicating the generation of more meso and micropores while doping and the pore radius of Cu-TiO_2/50-C_3N_4 is 4.38 nm.

3.5. XPS analysis

X-ray photoelectron spectra were collected to study the surface of the synthesized catalysts. The survey spectrum of P25 TiO_2 (Fig. 5 (a)) shows the presence of C, Ti and O and the survey spectrum of Cu-TiO_2 (Fig. 5 (b)) exhibits the presence of Cu in addition to C, Ti and O. The presence of C, N and O was revealed in the survey spectrum of g-C_3N_4 (Fig. 5 (c)) while the survey spectrum of Cu-TiO_2/50-C_3N_4 (Fig. 5 (d)) indicates the presence of all C, O, N, Ti and Cu. The higher-resolution spectra of the synthesized materials were collected to study sur-

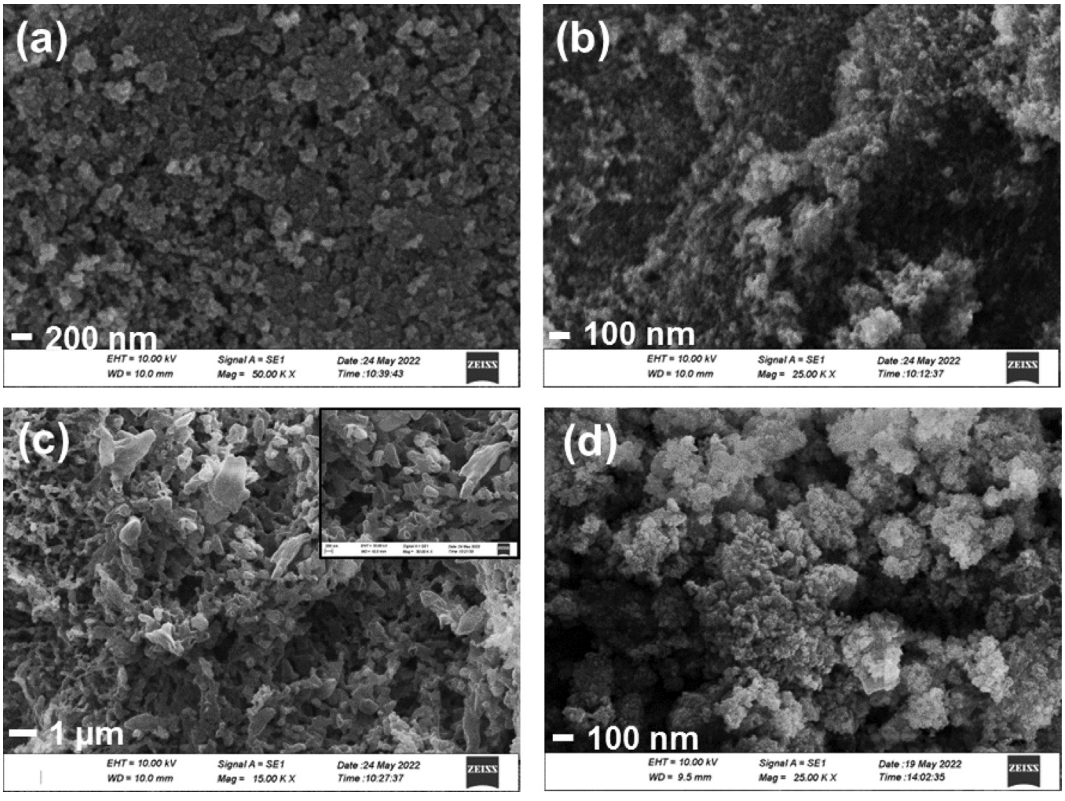

Fig. 4 SEM images of (a) P25 TiO_2 (b) Cu-TiO_2 (c) g-C_3N_4 (d) Cu-TiO_2/50- C_3N_4.

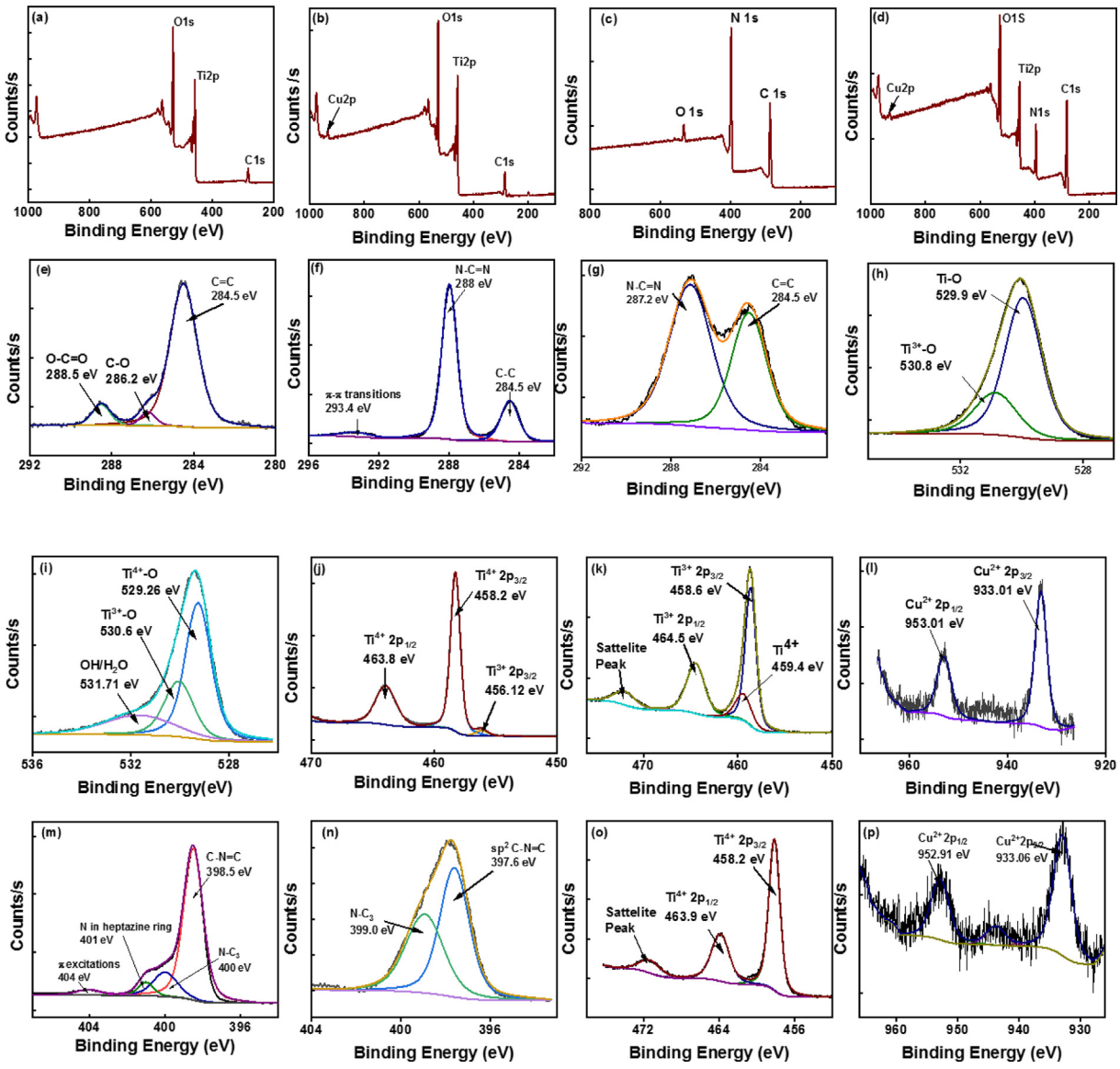

Fig. 5 Survey spectra of (a) P25 TiO_2 (b) Cu-TiO_2 (c) g-C_3N_4 (d) Cu-TiO_2/50-C_3N_4, C 1 s higher resolution spectrum of (e) P25 TiO_2 (f) g-C_3N_4 (g) Cu-TiO_2/50-C_3N_4, O 1 s higher resolution spectrum of (h) P25 TiO_2 (i) Cu-TiO_2, Ti 2p higher resolution spectrum of (j) P25 TiO_2 (k) Cu-TiO_2, of (l) Cu 2p higher resolution spectrum Cu-TiO_2, N 1 s higher resolution spectrum of (m) g-C_3N_4 (n) Cu-TiO_2/50-C_3N_4 (o) Ti 2p higher resolution spectrum of Cu-TiO_2/50-C_3N_4 (p) Cu 2p higher resolution spectrum of Cu-TiO_2/50-C_3N_4.

face chemistry in detail. The higher resolution spectrum of C 1 s of P25 TiO2 (Fig. 5 (e)) was deconvoluted to three peaks centered at 284.5, 286.2 and 288.5 eV which are attributed to sp^2 hybridized C=C, C-O and O-C=O, respectively. The higher resolution spectrum of C 1 s of g-C_3N_4 is given in Fig. 4 (f) and is deconvoluted to three main peaks centered at 284.5, 288 and 293.4 eV, which are attributed to the sp^2 hybridized graphitic C (C–C), sp^2 hybridized carbon in N-C=N and π-π transitions, respectively. Interestingly the two peaks appeared at 284.5 and 287.16 eV in the higher resolution spectrum of C 1 s of Cu-TiO_2/50-C_3N_4 (Fig. 5 (g) which were assigned to C=C and N-C=N, respectively. The binding energy of the peak corresponding to N-C = N has shifted to lower binding energy due to the interfacial interactions of g-C_3N_4 with Cu-TiO_2. The higher resolution spectrum of O 1 s of P25 TiO_2 (Fig. 5 (h)) is deconvoluted to two peaks at 529.95 and 530.85 eV. The peak at 529.95 eV is assigned to oxygen bound to Ti while the peak at 530.85 eV represents Ti_2O_3 further revealing the presence of both Ti^{4+} and Ti^{3+} in P25 TiO_2. The higher resolution spectrum of O 1 s of Cu-TiO_2 (Fig. 5 (i) is deconvoluted into three peaks at 529.26, 530.6 and 531.71 eV where the third new peak is attributed to the oxygen present in the hydroxyl group or physisorbed water. The higher resolution spectrum of Ti 2p of P25 TiO_2 (Fig. 5 (j)) shows the spin-orbital coupling where the $2p_{3/2}$ and $2p_{1/2}$ peaks of Ti^{4+} appeared at 458.2 and 463.8 eV, respectively, while the peak at 456.12 eV with low intensity corresponds to the $2p_{3/2}$ of Ti^{3+}. The appearance of Ti 2p peaks in the higher resolution spectrum of Ti 2p of Cu-TiO_2 (Fig. 5 (k)) is different to that of P25 TiO_2. The peak that appeared at 458.6 eV could be attributed to the Ti^{3+} and the peak at 459.4 eV could be assigned to the Ti^{4+} of TiO_2 and

the binding energy has shifted to higher values upon doping of Cu. As described in the XRD section Cu^{2+} replaces Ti^{4+} when Cu is doped to TiO_2 because the cationic radii are quite similar. However, once Cu^{2+} replaces the Ti^{4+} ,it creates a charge imbalance where an oxygen atom is also removed creating an oxygen vacancy to compensate for the balance. The most stable site to create the oxygen vacancy is the oxygen site neighbouring to the Cu dopant. Once an oxygen atom is removed the adjacent Cu and Ti ions to which the removed oxygen atom was bound would have five-fold coordination and thus produce the Ti^{3+} state (Mathew et al., 2018). The higher resolution spectrum of Cu 2p of Cu-TiO_2 (Fig. 5 (l)) shows the spin-orbital coupling where the $2p_{3/2}$ and $2p_{1/2}$ appeared at 933.26 and 953.01 eV, respectively, indicates the presence of Cu^{2+}. The higher resolution spectrum of N 1 s of g-C_3N_4 (Fig. 5 (m)) shows four sub-peaks at 398.5, 400, 401 and 404 eV, which are assigned to sp^2 hybridized N in s-triazine rings (C-N = C), N-C_3, N atoms in the heptazine ring and as bridging atom, and π-excitations, respectively. The higher resolution spectrum of N 1 s of Cu-TiO_2/50-C_3N_4 (Fig. 5 (n)) shows only two peaks at 397.6 and 399 eV in which the binding energies have decreased due to the interfacial linkage occurs between g-C_3N_4 and Cu-TiO_2 during the formation of the composite (Tan et al., 2015). The higher resolution spectrum of Ti 2p (Fig. 5 (o)) and Cu 2p (Fig. 5 (p)) of Cu-TiO_2/50-C_3N_4 shows the presence of Ti^{4+} (458.2 eV) and Cu^{2+} (933.06 eV), respectively, indicating that unstable Ti^{3+} has oxidized to Ti^{4+} in coupling with g-C_3N_4 during hydrothermal synthesis.

3.6. XRF analysis

XRF analysis was performed to understand the elemental composition. Six spots were chosen from each sample to perform the analysis to study the elemental distribution throughout the sample. TiO_2 purely contain only Ti as shown in Table 2. Cu-TiO_2 sample contains an average of 98.35 wt% of Ti and an average of 1.65 wt% of Cu where both the elements are uniformly distributed in all six places analyzed suggesting the homogeneous distribution of Cu on Ti. Therefore, it is evident that Cu has homogeneously doped to TiO_2 lattice.

3.7. UV–Visible diffuse reflectance spectroscopy

The optical absorption behaviours of the synthesized photocatalysts were evaluated by UV–Visible diffuse reflectance spectroscopy (Supplementary Figure 2 (a)). It could be seen that the TiO_2 exhibits the UV range with an absorption edge at 400 nm. The absorption edge of g-C_3N_4 appeared at 425 nm indicating the visible range absorption while that of Cu/TiO_2 is further shifted towards the visible range suggesting high visible light absorption. The behaviours of the absorption spectra of Cu-TiO_2/g-C_3N_4 were quite similar where they indicate visible light sensitivity of the heterojunctions. Tauc plots were constructed using the formula shown in equation 3 to determine the band gap of the synthesized nanomaterials.

$$(ahv)^n = A(hv - Eg) \quad (3)$$

Where hv, A, Eg and a represent the photon energy, absorption coefficient, band gap energy and a constant, respectively (Q. Li et al., 2007). n = 2 denotes the direct transitions and n = 1/2 indicates indirect transitions, and the plots corresponding to indirect and direct transitions are shown in Fig. 6 and Supplementary Figure 2 (b), respectively.

The behaviours of the plots suggest that the indirect transition is more feasible in the synthesized nanomaterials. The band gap of TiO_2 was 3.00 eV while that of g-C_3N_4 is 2.81 eV. The band gap of Cu-TiO_2 is found to be 2.67 eV exhibiting prominently visible absorption. A new energy level is created below the CB of TiO_2 narrowing down the band gap and further enhancing the visible light absorption. However, the band gap values of g-C_3N_4 coupled Cu-TiO_2 were higher than that of Cu-TiO_2 and were similar to each other and to that of g-C_3N_4. This could be due to the sample used for the analysis being more concentrated with g-C_3N_4. Further, the particle size directly contributes to the band gap whereas in general particle size is inversely proportional to the band gap. The size of the nanoparticles greatly affects the band gap where the band gap values increase as the particle size decreases. Holes in the valence band and electrons in the conduction band become confined with decreasing particle size and due to this confinement in the electrons and holes the band gap between the valence and conduction bands increases. The shape of the nanomaterials contributes to the band gap values. Volume to surface area ratio varies as the size and shape of the nanomaterials change which contributes to the variation in the number of surface atoms and hence the cohesive energy. Therefore, the band gap varies at the nanoscale due to the change in size and shape (Singh et al., 2018). Therefore, the obtained band gap values are a result of collective factors. It is evident that the coupled heterojunction composites are visible active for photocatalysis. All the calculated band gap values are tabulated in Table 3.

3.8. Photocatalysis

The photocatalytic activity of the synthesized nanomaterials was evaluated on the degradation of methylene blue under the exposure of UV and visible light. Before exposure to the light, source catalysts were shaken in dark for one hour to reach the adsorption–desorption equilibrium. Adsorption kinetics were studied using pseudo-first-order and

Table 2 XRF analysis of P25 TiO_2 and Cu-TiO_2.

Sample	Element	Spot 1 Mass %	Spot 2 Mass %	Spot 3 Mass %	Spot 4 Mass %	Spot 5 Mass %	Spot 6 Mass %
P25 TiO_2	Ti	100	100	100	100	100	100
Cu-TiO_2	Ti	98.38	98.31	98.38	98.38	98.31	98.31
	Cu	1.62	1.69	1.62	1.62	1.69	1.69

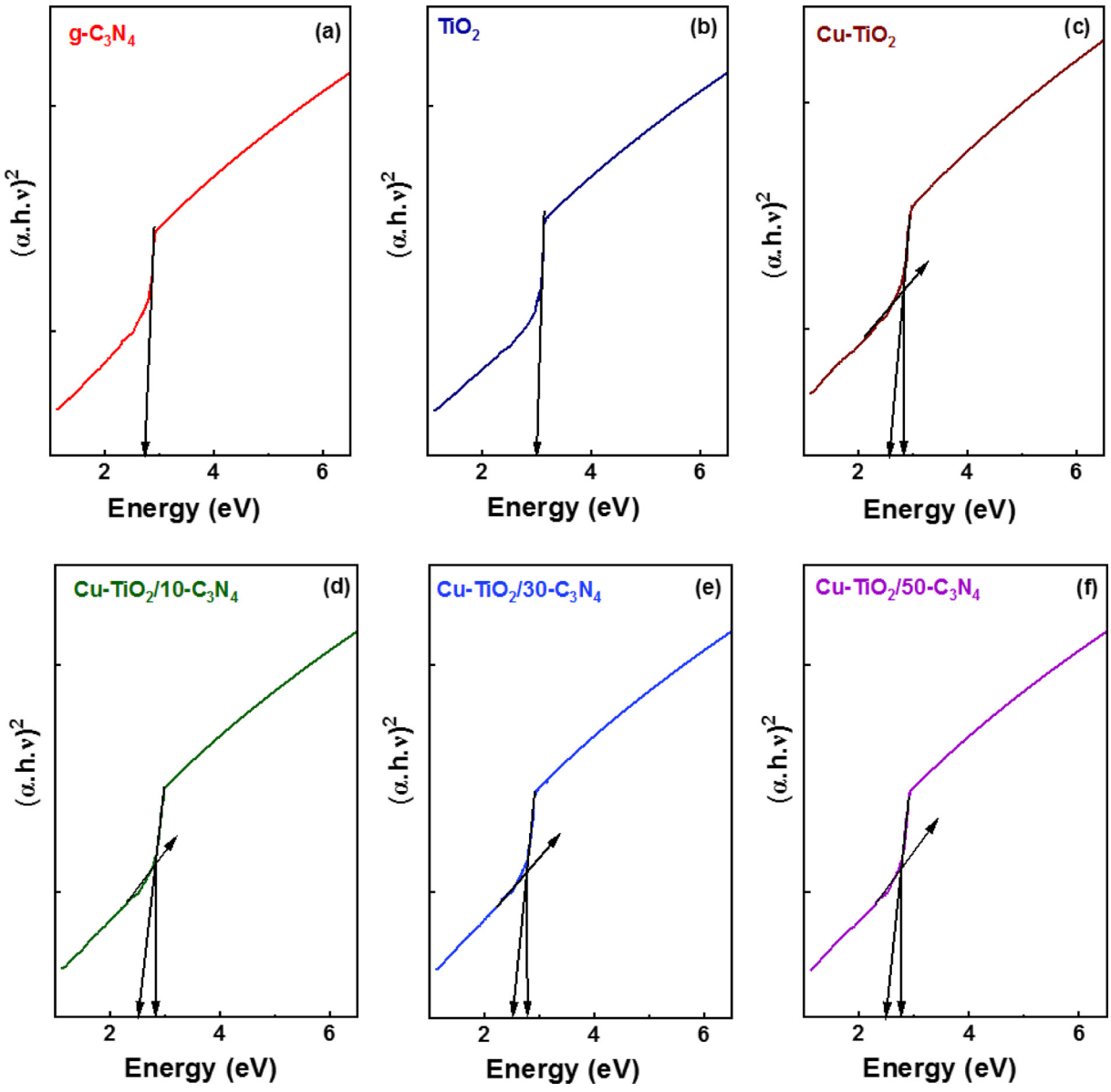

Fig. 6 Tauc plots indicating the indirect transitions of (a) g-C_3N_4 (b) TiO_2 (c) Cu-TiO_2 (d) Cu-TiO_2/10-C_3N_4 (e) Cu-TiO_2/30-C_3N_4 (f) Cu-TiO_2/50-C_3N_4.

pseudo-second-order kinetics models as shown in Fig. 7 (a) and (b). The respective rate constants and the correlation coefficient values are tabulated in Table 4. It is evident that the adsorption followed pseudo-second-order kinetics with a high R^2 value suggesting chemisorption of MB to the catalysts. Then the samples were exposed to the light source and the aliquots were withdrawn in 15 min time intervals (Fig. 8). Obtained data were fitted to the first-order kinetics model and the obtained data are tabulated in Table 5. Cu-TiO_2/50-C_3N_4 showed the highest rate constant (4.4×10^{-3} min^{-1}) for the photodegradation of MB followed by Cu-TiO_2/30-C_3N_4 (4.1×10^{-3} min^{-1}). The photocatalytic activity of Cu-TiO_2/50-C_3N_4 is 9.8 times greater than that of g-C_3N_4, 4 times greater than Cu-TiO_2 and 5 times greater than that of TiO_2. g-C_3N_4 is a visible active photocatalyst and the least photocatalytic activity was observed with g-C_3N_4 due to the electron-hole pair recombination. Pure TiO_2 is only active in the UV range leading to lower photocatalytic activity. Upon doping with Cu, the band gap reduces as a new energy level is constructed below the CB of TiO_2 increasing the visible light sensitivity. Therefore, the photocatalytic activity of Cu-TiO_2 is higher than that of TiO_2. Cu-TiO_2/C_3N_4 composites showed comparatively higher photocatalytic activity due to the proper band alignment which enhances the charge separation and the presence of two visibly active semiconductors, Cu-TiO_2 and g-C_3N_4. Photocatalytic activity of Cu-TiO_2/30-C_3N_4 and Cu-TiO_2/10-C_3N_4 was lower due to the low weight ratio between Cu-TiO_2 and g-C_3N_4 which leads to improper formation of the heterojunction. Therefore, it could be concluded that Cu-TiO_2/50-C_3N_4 is the most sustaining photocatalyst among the nanomaterials synthesized for the

Table 3 Band gap energies calculated for direct and indirect transitions of the synthesized nanomaterials.

Sample	Band Gap (eV) for direct transitions (n = 2)	Band Gap (eV) for indirect transitions (n = 1/2)
g-C_3N_4	2.73	2.81
TiO_2	3	3
Cu-TiO_2	2.59	2.67
Cu-TiO_2/10-C_3N_4	2.84	2.88
Cu-TiO_2/30-C_3N_4	2.78	2.84
Cu-TiO_2/50-C_3N_4	2.76	2.82

degradation of MB. MB was not degraded upon exposure to the light source without any catalyst as shown in the supplementary figure 3.

Mechanism of Photocatalysis

The engineering of the structure of the heterostructure is important to determine the mechanism of photocatalysis. The band gap values of Cu-TiO_2 and g-C_3N_4 calculated from the Tauc plots are 2.67 and 2.80 eV, respectively. The band edge potentials of the conduction band (E_{CB}) and the valence band (E_{VB}) of the above semiconductors were calculated by the formula (4) and (5), respectively.

$$ECB = X - EC - 0.5\,Eg\,. \quad (4)$$

$$EVB = X - EC + 0.5\,Eg\,. \quad (5)$$

where X is the electronegativity of the semiconductor, which is the geometric mean of the electronegativity of the constituent atoms, and E^C is the energy of the free electrons on the hydrogen scale which is approximately 4.5. X value for Cu-TiO_2 is assumed to be similar to that of TiO_2 (5.81) as the percentage of Cu incorporated is low compared to Ti (1%) and that of g-C_3N_4 is 4.73. E_{CB} calculated for TiO_2 (Rutile), TiO_2 (Anatase) Cu-TiO_2 and g-C_3N_4 are −0.19, −0.39, −0.03 and − 1.18 eV/normal hydrogen electrode (NHE), respectively, and the E_{VB} calculated are 2.81, 2.81, 2.65, and 1.64 eV/normal hydrogen electrode (NHE), respectively. A homojunction was established between the Rutile and Anatase phases of P25 TiO_2 as shown in Fig. 9 (a) where the CB band of Rutile lies below that of Anatase facilitating the migration of electrons from the CB of Anatase to that of Rutile. The potential of the VB of both TiO_2 Rutile and Anatase (2.81 eV) is greater than that of the standard potential of $OH^{\bullet}/OH^-$ (1.99 eV) and $OH^{\bullet}/H_2O$ (2.68 eV) facilitating the oxidation of both OH^- and H_2O to produce $OH^{\bullet}$. Further, the potential of the CB of TiO_2 (Anatase) (-0.39 eV) is greater than that of the standard potential of $O_2/O_2^{-\bullet}$ (-0.33 eV) favouring the reduction of O_2 to $O_2^{-\bullet}$. However, the potential of the CB of TiO_2 (Rutile) (-0.19 eV) is smaller than the standard potential of $O_2/O_2^{-\bullet}$ and hence prohibits the reduction of O_2 to $O_2^{-\bullet}$. Further, as the potential of the CB of TiO_2 (Rutile) is lower than that of TiO_2 (Anatase) there is a net electron transfer from the CB of TiO_2 (Anatase) to the CB of TiO_2 (Rutile). Hence, the probability of the reduction of O_2 to $O_2^{-\bullet}$ is lower than expected. Therefore, such produced $OH^{\bullet}$ and $O_2^{-\bullet}$ degrade the MB molecules in the presence of UV light. As discussed in the XRD analysis Cu^{2+} ions have been mainly doped to the TiO_2 (Anatase) phase of P25 TiO_2 lowering the band gap to 2.67 eV and the CB of Cu-TiO_2 lies at −0.03 eV while the VB would be located at 2.64 eV cresting a type I heterojunction. Further, the electrons will travel from the CB of TiO_2 (Rutile) to the CB band of Cu-TiO_2 while the holes will migrate from the VB of the TiO_2 (Rutile) to the VB of Cu-TiO_2 and hence cause electron hole pair recombination leading to poor charge separation. The oxidation of H_2O to $OH^{\bullet}$ is feasible at the VB of TiO_2 (Rutile) but would occurrence be limited as the holes are migrated to the VB of Cu-TiO_2 due to the favourable potential difference as shown in Fig. 9 (b). The oxidation of OH^- to $OH^{\bullet}$ is favourable and occurs at high probability at the VB of Cu-TiO_2 due to the flow of holes to the VB of Cu-TiO_2. Hence, $OH^{\bullet}$ contribute to the degradation of MB by Cu-TiO_2. The photocatalytic activity of this photocatalyst is comparatively higher than that of both pure TiO_2 and g-C_3N_4 due to its high visible activity. The electrons which migrated to the CB of the Cu-TiO_2 from TiO_2 (Rutile) then travelled to the VB of g-C_3N_4 of Cu-TiO_2/C_3N_4 as the z-scheme band alignment created due to the potential difference of the CB of Cu-TiO_2 and the VB of g-C_3N_4

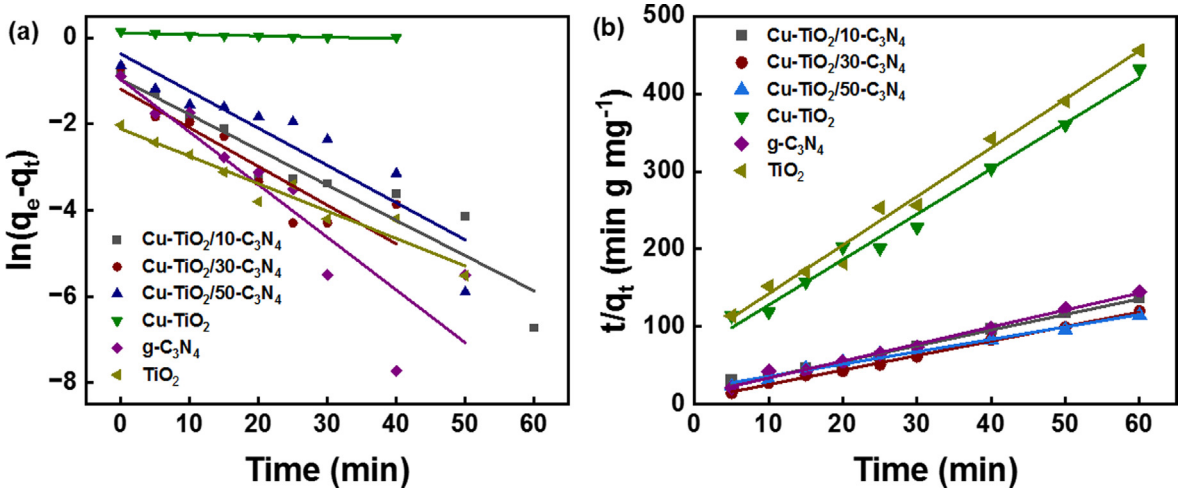

Fig. 7 (a) Pseudo-first-order (b) Pseudo-second-order adsorption kinetic model for adsorption of MB to the synthesized nanomaterials.

Table 4 Kinetics parameters for adsorption of MB to the synthesized nanomaterials.

Sample	1st order rate constant (min^{-1})	R^2	2nd Order rate Constant ($mg\ g^{-1}\ min^{-1}$)	R^2
Cu-TiO_2/10-C_3N_4	0.091	0.89	0.243	0.99
Cu-TiO_2/30-C_3N_4	0.107	0.79	0.436	0.99
Cu-TiO_2/50-C_3N_4	0.100	0.82	0.122	0.98
Cu-TiO_2	0.004	0.8	0.479	0.99
g-C_3N_4	0.144	0.79	0.345	0.99
TiO_2	0.070	0.93	0.481	0.99

Table 5 Kinetics parameters for photocatalytic degradation of MB in the presence of the synthesized catalysts.

Sample	1st Order rate constant (min^{-1})	R^2	1st Order rate constant in the presence of 4 mM persulfate (min^{-1})
Cu-TiO_2/10-C_3N_4	3.9×10^{-3}	0.99	4.9×10^{-2}
Cu-TiO_2/30-C_3N_4	4.1×10^{-3}	0.99	1.3×10^{-1}
Cu-TiO_2/50-C_3N_4	4.4×10^{-3}	0.99	7.9×10^{-2}
Cu-TiO_2	1.1×10^{-3}	0.99	5.6×10^{-2}
g-C_3N_4	4.5×10^{-4}	0.97	6.3×10^{-2}
TiO_2	8.7×10^{-4}	0.99	4.9×10^{-2}

favour the electron transfer. Additional to the reactions occurred at Cu-TiO_2 electrons at the VB of g-C_3N_4 get excited to the CB and the reduction of O_2 to $O_2^{\bullet}$ happens at the CB of g-C_3N_4 as the potential of the CB of g-C_3N_4 (-1.18 eV) is greater than the reduction potential of $O_2/O_2^{\bullet}$. Hence, both $OH^{\bullet}$ and $O_2^{\bullet}$ are responsible for the degradation of MB in the presence of Cu-TiO_2/C_3N_4 as the photocatalyst.

Cu-TiO_2/50 g-C_3N_4 showed the highest rate constant (4.4×10^{-3} min^{-1}) due to the proper ratio of mixing Cu-TiO_2 with g-C_3N_4. Composites made with other ratios where 10% and 30% g-C_3N_4 were coupled with Cu-TiO_2 also effectively contributed to the photodegradation of MB but with lesser activity as the heterojunctions with the proper ratio were not formed. The rate constant per surface area of Cu-TiO_2/50 g-C_3N_4 (1.24×10^{-4} $min^{-1}/m^2.g^{-1}$) is greater than that of Cu-TiO_2 (1.3 x10^{-5} $min^{-1}/m^2.g^{-1}$) and TiO_2 (7.8×10^{-6} $min^{-1}/m^2.g^{-1}$) further indicate that the coupling of Cu-TiO_2 with g-C_3N_4 has greatly enhanced the photocatalytic activity.

XPS analysis further supports the above-proposed mechanism. The higher resolution spectrum of N1s of Cu-TiO_2/50-C_3N_4 showed 0.9 eV and 1.0 eV downshifts of the binding energy of the peaks corresponding to C-N = C and N-C_3, respectively, compared to those of pure g-C_3N_4 indicating an increase in the electron density. Hence, those electrons present in the CB of g-C_3N_4 of Cu-TiO_2/50-C_3N_4 are taken by the O_2 and get reduced to $O_2^{\bullet}$ which converts MB to harmless products (Thambiliyagodage, Usgodaarachchi, et al., 2022). Further, the binding energy of Ti 2p of Ti^{4+} of Cu-TiO_2/50-

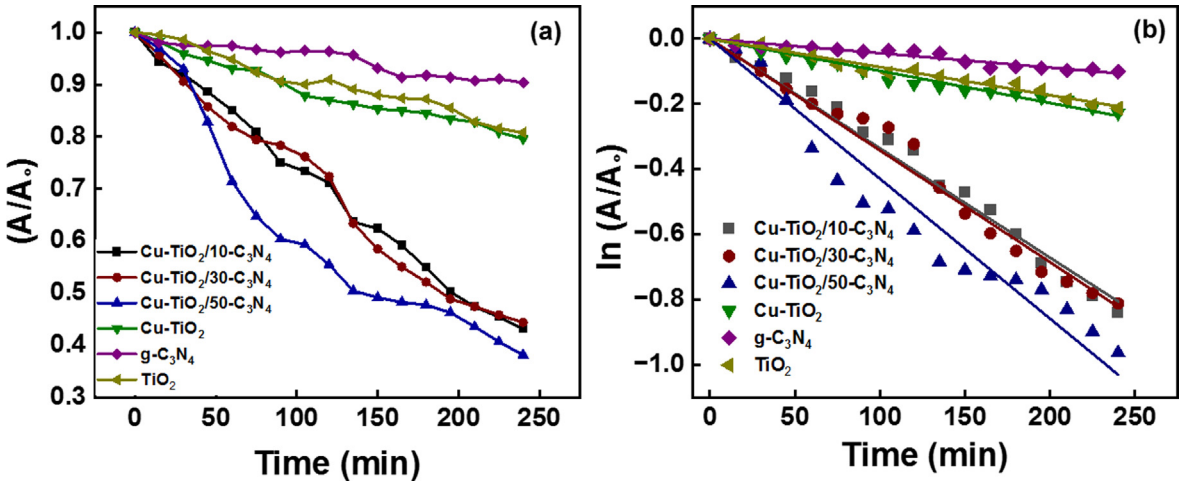

Fig. 8 Photocatalytic degradation of MB in the presence of the synthesized photocatalysts following (a) photocatalytic degradation (b) pseudo-first-order kinetics model.

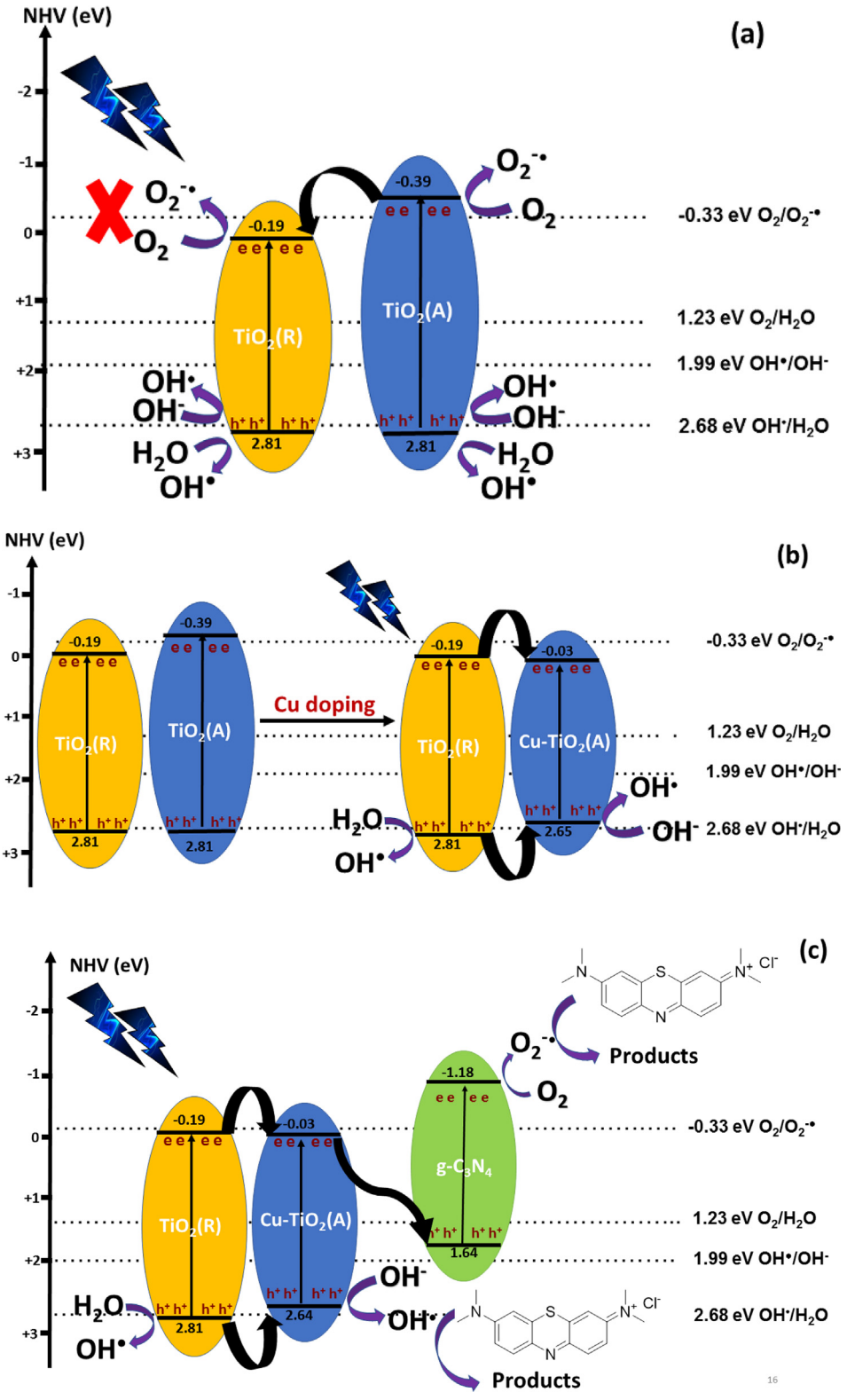

Fig. 9 Band alignment of (a) P25 TiO_2 (b) Cu-TiO_2 (c) Cu-TiO_2/g-C_3N_4.

C_3N_4 shows a 1.2 eV downshift compared to that of Cu-TiO_2, while a 0.2 eV downshift in the Cu 2p was also observed in Cu-TiO_2/50-C_3N_4 compared to Cu-TiO_2. This indicates an increase in the electron density in the CB of Cu-TiO_2 of Cu-TiO_2/50-C_3N_4 which is due to the electron flow from g-C_3N_4 as suggested by described band alignment. Higher resolution spectra of Cu-TiO_2/50-C_3N_4 used for the photocatalytic reaction (Cu-TiO_2/50-C_3N_4 – L) were acquired to further support the charge transfer mechanism. The higher resolution spectrum of Ti 2p Cu-TiO_2/50-C_3N_4 – L was deconvoluted into five

peaks as shown in supplementary figure 4 (a). The peak at 458.7 eV is attributed to the Ti^{3+} while the peak at 460.9 eV is ascribed to Ti^{4+} of Ti $2p_{3/2}$. The peaks at 464.4 and 466.5 eV correspond to the $2p_{1/2}$ of the Ti^{3+} and Ti^{4+}, respectively. Though only Ti^{4+} was present in the Cu-TiO_2/50-C_3N_4 interestingly both Ti^{3+} and Ti^{4+} were present in the same catalyst which was exposed to the photocatalytic reaction. As shown in Fig. 9 photogenerated electrons in the VB band of TiO_2 (Rutile) are transferred to the VB of TiO_2 (Anatase) and hence the Ti^{4+} of anatase reduced to Ti^{3+} greatly where the ratio of Ti^{4+}/ Ti^{3+} is 1:2 indicating that 2/3 of Ti^{4+} have been reduced to Ti^{3+} when exposed to the reaction in the presence of the light source. The higher resolution spectrum of N 1 s of Cu-TiO_2/50-C_3N_4 – L (supplementary figure 4 (b)) was deconvoluted to three peaks where an additional peak at 398.5 eV corresponding to N in the pyridine ring appeared which indicates the adsorption of MB molecules to the catalyst surface during the catalytic reaction as the MB molecule possesses a pyridine ring in its structure (supplementary figure 5).

To identify the reactive species, the study was conducted in the presence of EDTA and IPA as they scavenge the holes and $OH^{\bullet}$, respectively. The rate constant for the photodegradation of MB decreased to 3.2×10^{-4} and 2.9×10^{-3} min^{-1}, respectively, in the presence of EDTA and IPA which are 13.8 and 1.5 times lesser than the rate constant when no scavenger is used (4.4×10^{-3} min^{-1}) (Fig. 10 (a)). The percentage conversion of MB in the presence of EDTA and IPA reduced to 8 and 48 %, respectively, indicating that both holes and $OH^{\bullet}$ have contributed to the photodegradation of MB where the effect from holes for the photocatalysis is 9.1 times greater than that from $OH^{\bullet}$ (Fig. 10 (b)).

The rate constant was increased to 7.9×10^{-2} min^{-1} with the addition of persulfate ($S_2O_8^{2-}$) ions to the medium which increased the rate by 18 times because the $SO_4^{\bullet-}$ and $OH^{\bullet}$ produced by the reduction of $S_2O_8^{2-}$ readily degrade MB increasing the conversion of MB to 98% compared to 62 % resulted when persulfate was not used. $S_2O_8^{2-}$ ions are reduced to $SO_4^{\bullet-}$ as shown in reaction 1 by the photogenerated electrons and such produced $SO_4^{\bullet-}$ reacts with OH^- in the medium to produce SO_4^{2-} and $OH^{\bullet}$ (reaction 2). Further, in the presence of UV light $S_2O_8^{2-}$ degrades to produce $2SO_4^{\bullet-}$ (reaction 3) which would react with OH^- to produce $OH^{\bullet}$. Moreover, in the presence of $O_2^{\bullet-}$, $S_2O_8^{2-}$ produce SO_4^{2-}, $SO_4^{\bullet-}$ and O_2 as shown in reaction 4. Additionally, the standard reduction potential of $S_2O_8^{2-}/2SO_4^{\bullet-}$ (2.01 eV) is lesser than E_{VB} of Cu-TiO_2, the longer O-O bond (1.497 Å) and easiness to break the O-O bond with less energy to produce $OH^{\bullet}$, making $S_2O_8^{2-}$ a better candidate to improve the reaction rate. The concentration of $S_2O_8^{2-}$ was varied as 2, 4 and 8 mM to study the optimum concentration of $S_2O_8^{2-}$ and the rate constants for the photodegradation of MB were calculated to be 5.6×10^{-2}, 7.9×10^{-2} and 1.2×10^{-1} min^{-1}, respectively (Fig. 10 (c)).

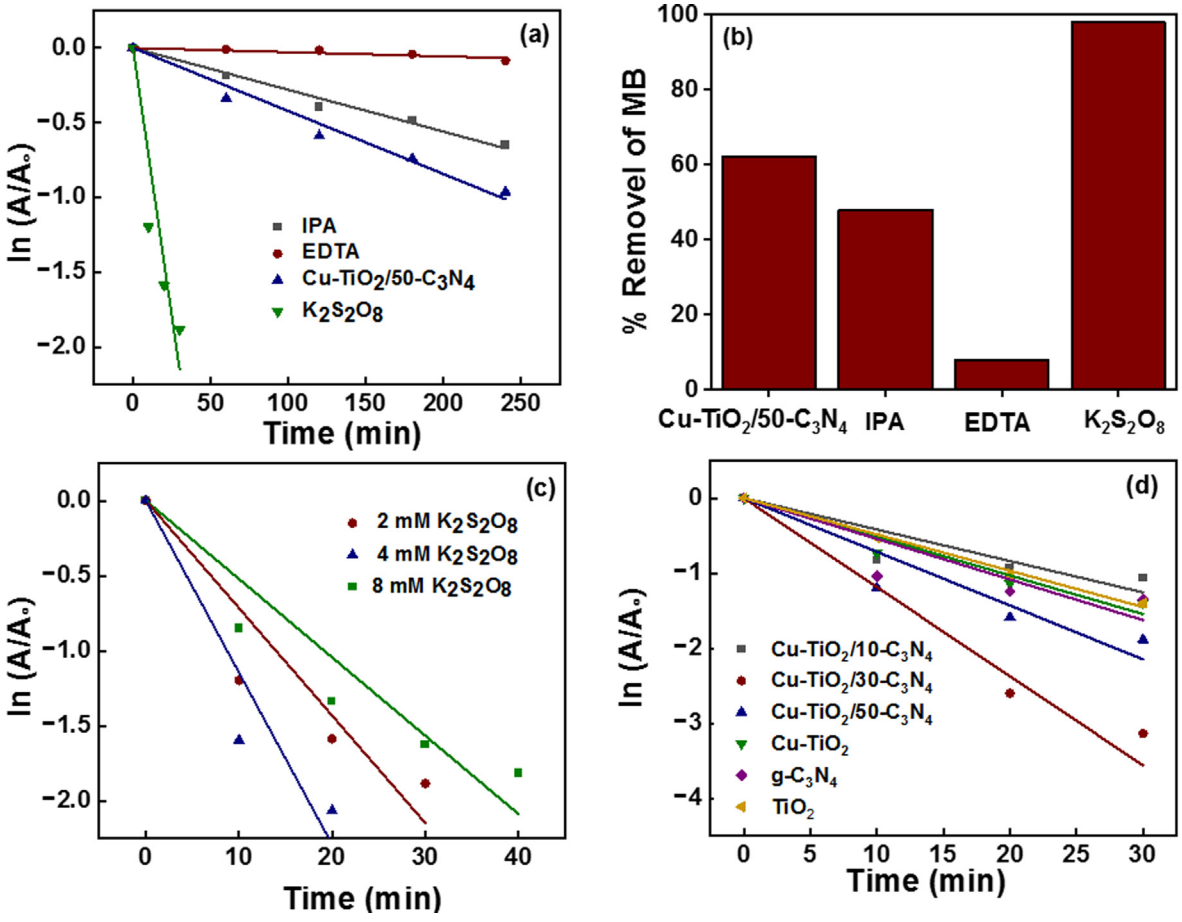

Fig. 10 (a) First order kinetics model for the catalytic system with additives; IPA, EDTA, $K_2S_2O_8$, and no additive (b) % removal of MB with the additives (c) First order kinetics model for the catalytic system with varying concentrations of $K_2S_2O_8$, (d) effect of $K_2S_2O_8$ on all the catalytic systems.

The rate constant increased with increasing concentration of $S_2O_8^{2-}$ as the concentrations of produced $SO_4^{\bullet}$ and $OH^{\bullet}$ increase with increasing concentration of $S_2O_8^{2-}$.

$$S_2O_8^{2-} + e^- \rightarrow SO_4^{-\bullet} + SO_4^{2-} \quad (1)$$

$$SO_4^{-\bullet} + OH^- \rightarrow SO_4^{2-} + OH^{\bullet} \quad (2)$$

$$S_2O_8^{2-} + h\nu \rightarrow 2\ SO_4^{-\bullet} \quad (3)$$

$$S_2O_8^{2-} + O_2^{-\bullet} \rightarrow SO_4^{2-} + SO_4^{-\bullet} + O_2 \quad (4)$$

Moreover, the effect of $S_2O_8^{2-}$ on the photocatalytic activity in the presence of all the synthesized photocatalysts was determined using 4 mM $S_2O_8^{2-}$ solution and the obtained rate constants are tabulated in Table 5. It is observed that the rate constants increased by 13, 32,51,140 and 56 times in the presence of Cu-TiO_2/10-C_3N_4, Cu-TiO_2/30-C_3N_4, Cu-TiO_2, g-C_3N_4 and TiO_2, respectively, suggesting that the photocatalysis is greatly increased due to two reasons mainly, which are the production of $SO_4^{\bullet}$ and $OH^{\bullet}$ which readily degrade MB molecules and the prevention of electron-hole pair recombination due to rapid capture of the photogenerated electrons by $S_2O_8^{2-}$ (Fig. 10 (d)). A drastic increase in the reaction rate in the presence of Cu-TiO_2/10-C_3N_4, Cu-TiO_2/30-C3N4, Cu-TiO_2, g- C_3N_4 and TiO_2 catalysts was observed in the presence of $S_2O_8^{2-}$ because the rate constants without $S_2O_8^{2-}$ were very low. The rate constants for the degradation of MB in the presence of all the composites are higher than that of Cu-TiO_2/50-C_3N_4 reported without $S_2O_8^{2-}$. Further, with the addition of $S_2O_8^{2-}$ the photocatalytic activity of Cu-TiO_2/30-C_3N_4 resulted to be higher than that of Cu-TiO_2/50-C_3N_4 which showed the highest photocatalytic activity without $S_2O_8^{2-}$. This suggests that the proper amount of g-C_3N_4 was not available in Cu-TiO_2/30-C_3N_4 to couple with Cu-TiO_2 and a low photocatalytic activity next to Cu-TiO_2/50-C_3N_4 was obtained due to the possible electron-hole pair recombination resulted due to the reduced band gap of Cu-TiO_2 (2.67 eV). However, $S_2O_8^{2-}$ readily captures the photogenerated electrons, and thus prevents the electron-hole pair recombination leading to a higher photocatalytic activity.

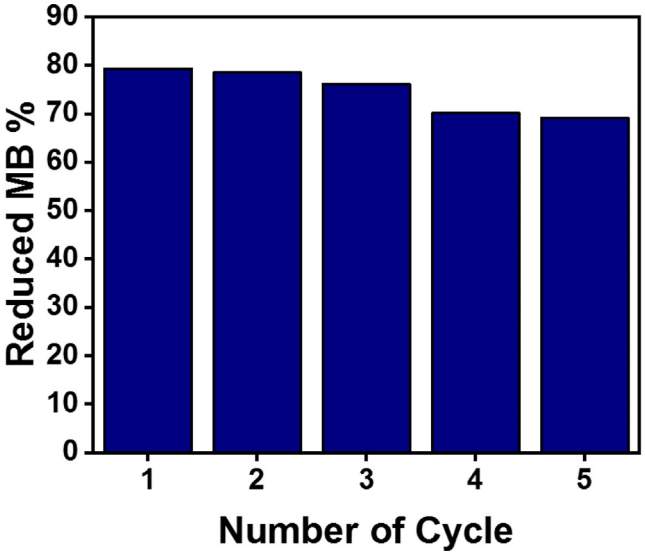

Fig. 11 Reusability of Cu-TiO_2/50-C_3N_4.

The reusability of Cu-TiO_2/50- C_3N_4 was tested to study the stability of the photocatalysts (Fig. 11). The total removal of MB in the first cycle (79%) decreased to 69% by the fifth cycle. Positively charged MB molecules have a strong affinity to the negatively charged catalyst surface triggering the chemisorption of MB. Therefore, the catalyst surface could have been saturated by the chemisorbed MB molecules limiting the available surface for the new MB molecules though the catalyst surface was washed with distilled water and ethanol because such washing would mainly remove the physisorbed MB molecules. The porous structure of the catalyst could have been blocked with the chemisorbed MB molecules reducing the surface area and the total pore volume limiting the MB adsorption. Moreover, it was observed that the catalyst particles were agglomerated with prolonged use reducing the surface area and restricting the access of MB molecules to the active sites. Further, there could be a loss in the weight of the catalyst moving from one cycle to the other resulting in a reduction in the total removal of MB.

4. Conclusions

Cu-TiO_2 nanoparticles were successfully coupled to g-C_3N_4 in different weight ratios hydrothermally to synthesize Cu-TiO_2/g-C_3N_4 nanocomposites. Cu has been doped to the Anatase phase of TiO_2 which possess both Anatase and Rutile phases without causing significant lattice distortions. Cu-TiO_2 nanoparticles were heterogeneously distributed on the g- C_3N_4 matrix. Adsorption of methylene blue molecules followed second-order kinetics indicating chemisorption of methylene blue molecules to the catalyst surface. The photocatalytic activity of the synthesized nanocomposites was evaluated on the photodegradation of methylene blue and Cu-TiO_2/50- C_3N_4 showed the highest rate constant (4.4×10^{-3} min^{-1}) which was 5 and 9.8 times greater the activity of TiO_2 and g-C_3N_4, respectively. The z-scheme band alignment of Cu-TiO_2/C_3N_4 facilitates the charge separation minimizing the electron-hole pair recombination and leading to higher photocatalytic activity. Superoxide radicals, hydroxyl radicals and holes are responsible for the photodegradation of methylene blue as exhibited by the study performed with scavengers. Persulfate ions greatly enhanced the photocatalytic activity where the rate constant of Cu-TiO_2/50-C_3N_4 was increased by 18 times as they generate $SO_4^{\bullet}$ and $OH^{\bullet}$ and prevent the electron-hole pair recombination. Therefore, it could be concluded that the fabricated Cu-TiO_2/C_3N_4 nanocomposites are effective in degrading methylene blue and could be used for environmental remediation effectively.

Declaration of Competing Interest

The authors declare that they have no known competing financial interests or personal relationships that could have appeared to influence the work reported in this paper.

Acknowledgement

The authors acknowledge the Sri Lanka Institute of Nanotechnology and the University of Moratuwa for providing the instrument facilities.

Funding Statement

This research was supported by the Accelerating Higher Education Expansion and Development (AHEAD) Operation of the Ministry of Higher Education funded by the World Bank.

Appendix A. Supplementary data

Supplementary data to this article can be found online at https://doi.org/10.1016/j.arabjc.2023.104749.

References

Al-Tohamy, R., Ali, S.S., Li, F., Okasha, K.M., Mahmoud, Y.A.G., Elsamahy, T., Jiao, H., Fu, Y., Sun, J., 2022. A critical review on the treatment of dye-containing wastewater: Ecotoxicological and health concerns of textile dyes and possible remediation approaches for environmental safety. Ecotoxicol. Environ. Saf. 231,. https://doi.org/10.1016/J.ECOENV.2021.113160 113160.

Azanaw, A., Birlie, B., Teshome, B., Jemberie, M., 2022. Textile effluent treatment methods and eco-friendly resolution of textile wastewater. Case Studies in Chemical and Environmental Engineering 6,. https://doi.org/10.1016/J.CSCEE.2022.100230 100230.

Babar, M., Munir, H.M.S., Nawaz, A., Ramzan, N., Azhar, U., Sagir, M., Tahir, M.S., Ikhlaq, A., Mohammad Azmin, S.N. huda, Mubashir, M., Khoo, K.S., Chew, K.W., 2022. Comparative study of ozonation and ozonation catalyzed by Fe-loaded biochar as catalyst to remove methylene blue from aqueous solution. Chemosphere 307,. https://doi.org/10.1016/J.CHEMOSPHERE.2022.135738 135738.

Balachandran, U., Eror, N.G., 1982. Raman spectra of titanium dioxide. J. Solid State Chem. 42 (3), 276–282. https://doi.org/10.1016/0022-4596(82)90006-8.

Bezzerrouk, M.A., Bousmaha, M., Hassan, M., Akriche, A., Kharroubi, B., Naceur, R., Guezzoul, M., 2021. Enhanced methylene blue removal efficiency of SnO2 thin film using sono-photocatalytic processes. Opt. Mater. 117,. https://doi.org/10.1016/J.OPTMAT.2021.111116 111116.

Birniwa, A. H., Abubakar, A. S., Mahmud, H. N. M. E., Kutty, S. R. M., Jagaba, A. H., Abdullahi, S. S., & Zango, Z. U. 2022. Application of Agricultural Wastes for Cationic Dyes Removal from Wastewater. 239–274. https://doi.org/10.1007/978-981-19-2832-1_9.

Charitha, T., Leshan, U., Shanitha, M., Ramanee, W., Buddi, L., Martin, B., 2021. Efficient photodegradation activity of α-Fe2O3/Fe2TiO5/TiO2 and Fe2TiO5/TiO2 nanocomposites synthesized from natural ilmenite. Results in Materials 12,. https://doi.org/10.1016/J.RINMA.2021.100219 100219.

Dutta, S., Bhattacharjee, J., 2022. A comparative study between physicochemical and biological methods for effective removal of textile dye from wastewater. Development in Wastewater Treatment Research and Processes 1–21. https://doi.org/10.1016/B978-0-323-85657-7.00003-1.

Faria, P.C.C., Órfão, J.J.M., Figueiredo, J.L., Pereira, M.F.R., 2008. Adsorption of aromatic compounds from the biodegradation of azo dyes on activated carbon. Appl. Surf. Sci. 254 (11), 3497–3503. https://doi.org/10.1016/J.APSUSC.2007.11.043.

Fawzi Suleiman Khasawneh, O., Palaniandy, P., 2021. Removal of organic pollutants from water by Fe2O3/TiO2 based photocatalytic degradation: A review. Environ. Technol. Innov. 21,. https://doi.org/10.1016/J.ETI.2020.101230 101230.

Geng, X., Wang, L., Zhang, L., Wang, H., Peng, Y., Bian, Z., 2021. H2O2 production and in situ sterilization over a ZnO/g-C3N4 heterojunction photocatalyst. Chem. Eng. J. 420,. https://doi.org/10.1016/J.CEJ.2021.129722 129722.

Ghosh, M., Liu, J., Chuang, S.S.C., Jana, S.C., 2018. Fabrication of Hierarchical V2O5 Nanorods on TiO2 Nanofibers and Their Enhanced Photocatalytic Activity under Visible Light. ChemCatChem 10 (15), 3305–3318. https://doi.org/10.1002/CCTC.201800172.

Gunathilaka, H., Thambiliyagodage, C., Usgodaarchchi, L., Angappan, S., 2021. Effect of surfactants on morphology and textural parameters of silica nanoparticles derived from paddy husk and their efficient removal of methylene blue. International Conference on Innovations in Energy Engineering & Cleaner Production IEE CP 21. https://doi.org/10.6084/m9.figshare.14904873.

Guo, Q., Zhou, C., Ma, Z., Yang, X., 2019. Fundamentals of TiO2 Photocatalysis: Concepts, Mechanisms, and Challenges. Adv. Mater. 31 (50), 1901997. https://doi.org/10.1002/ADMA.201901997.

Hardcastle, F.D., 2011. Raman Spectroscopy of Titania (TiO 2) Nanotubular Water-Splitting Catalysts. In Journal of the Arkansas Academy of. Science 65 (9) http://scholarworks.uark.edu/-jaashttp://scholarworks.uark.edu/jaas/vol65/iss1/9.

Ihaddaden, S., Aberkane, D., Boukerroui, A., Robert, D., 2022. Removal of methylene blue (basic dye) by coagulation-flocculation with biomaterials (bentonite and Opuntia ficus indica). J. Water Process Eng. 49,. https://doi.org/10.1016/J.JWPE.2022.102952 102952.

J. Thambiliyagodage, C., Hakat, Y., & G. Bakker, M. 2016. One Pot Synthesis of Carbon/Ni Nanoparticle Monolithic Composites by Nanocasting and Their Catalytic Activity for 4-Nitrophenol Reduction. Current Catalysis, 5(2), 135–146. https://doi.org/10.2174/2211544705666160610093114.

Javanbakht, V., Mohammadian, M., 2021. Photo-assisted advanced oxidation processes for efficient removal of anionic and cationic dyes using Bentonite/TiO2 nano-photocatalyst immobilized with silver nanoparticles. J. Mol. Struct. 1239,. https://doi.org/10.1016/J.MOLSTRUC.2021.130496 130496.

Jing, D., Guo, L., 2007. WS2 sensitized mesoporous TiO2 for efficient photocatalytic hydrogen production from water under visible light irradiation. Catal. Commun. 8 (5), 795–799. https://doi.org/10.1016/J.CATCOM.2006.09.009.

Kirchon, A., Zhang, P., Li, J., Joseph, E.A., Chen, W., Zhou, H.C., 2020. Effect of Isomorphic Metal Substitution on the Fenton and Photo-Fenton Degradation of Methylene Blue Using Fe-Based Metal-Organic Frameworks. ACS Appl. Mater. Interfaces 12 (8), 9292–9299. https://doi.org/10.1021/ACSAMI.9B21408/SUPPL_FILE/AM9B21408_SI_001.PDF.

Kobkeatthawin, T., Chaveanghong, S., Trakulmututa, J., Amornsakchai, T., Kajitvichyanukul, P., & Smith, S. M. (2022). Photocatalytic Activity of TiO2/g-C3N4 Nanocomposites for Removal of Monochlorophenols from Water. Nanomaterials 2022, Vol. 12, Page 2852, 12(16), 2852. https://doi.org/10.3390/NANO12162852.

Lakshmana Reddy, N., Emin, S., Valant, M., Shankar, M.V., 2017. Nanostructured Bi2O3@TiO2 photocatalyst for enhanced hydrogen production. Int. J. Hydrogen Energy 42 (10), 6627–6636. https://doi.org/10.1016/J.IJHYDENE.2016.12.154.

Lee, H., Jang, H.S., Kim, N.Y., Joo, J.B., 2021. Cu-doped TiO2 hollow nanostructures for the enhanced photocatalysis under visible light conditions. J. Ind. Eng. Chem. 99, 352–363. https://doi.org/10.1016/J.JIEC.2021.04.045.

Lellis, B., Fávaro-Polonio, C.Z., Pamphile, J.A., Polonio, J.C., 2019. Effects of textile dyes on health and the environment and bioremediation potential of living organisms. Biotechnology Research and Innovation 3 (2), 275–290. https://doi.org/10.1016/J.BIORI.2019.09.001.

Li, T., Abdelhaleem, A., Chu, W., Pu, S., Qi, F., Zou, J., 2021b. S-doped TiO2 photocatalyst for visible LED mediated oxone activation: Kinetics and mechanism study for the photocatalytic degradation of pyrimethanil fungicide. Chem. Eng. J. 411,. https://doi.org/10.1016/J.CEJ.2021.128450 128450.

Li, H., Wu, C.H., Liu, Y.C., Yuan, S.H., Chiang, Z.X., Zhang, S., Wu, R.J., 2021a. Mesoporous WO3-TiO2 heterojunction for a hydrogen gas sensor. Sens. Actuators B 341,. https://doi.org/10.1016/J.SNB.2021.130035 130035.

Li, Q., Xie, R., Yin, W.L., Mintz, E.A., Jian, K.S., 2007. Enhanced visible-light-induced photocatalytic disinfection of E. coli by carbon-sensitized nitrogen-doped titanium oxide. Environ. Sci. Tech. 41 (14), 5050–5056. https://doi.org/10.1021/es062753c.

Li, X., Zhang, H., Ma, F., Cheng, S., Shen, Z., Zhang, J., Min, J., Wang, Y., Liu, G., Yao, H., 2021c. Electro-catazone treatment of ozone-resistant drug ibuprofen: Interfacial reaction kinetics, influencing mechanisms, and degradation sites. Journal of Hazardous Materials Advances 4,. https://doi.org/10.1016/J.HAZADV.2021.100023 100023.

Liao, X., Li, T.T., Ren, H.T., Zhang, X., Shen, B., Lin, J.H., Lou, C. W., 2022. Construction of BiOI/TiO2 flexible and hierarchical S-scheme heterojunction nanofibers membranes for visible-light-driven photocatalytic pollutants degradation. Sci. Total Environ. 806,. https://doi.org/10.1016/J.SCITOTENV.2021.150698 150698.

Lu, C., Yang, J., Khan, A., Yang, J., Li, Q., Wang, G., 2022. A highly efficient technique to simultaneously remove acidic and basic dyes using magnetic ion-exchange microbeads. J. Environ. Manage. 304,. https://doi.org/10.1016/J.JENVMAN.2021.114173 114173.

Lyu, L., Zhang, L., Hu, C., Yang, M., 2016. Enhanced Fenton-catalytic efficiency by highly accessible active sites on dandelion-like copper–aluminum–silica nanospheres for water purification. J. Mater. Chem. A 4 (22), 8610–8619. https://doi.org/10.1039/C6TA02276F.

Mathew, S., Ganguly, P., Rhatigan, S., Kumaravel, V., Byrne, C., Hinder, S., Bartlett, J., Nolan, M., Pillai, S., 2018. Cu-Doped TiO2: Visible Light Assisted Photocatalytic Antimicrobial Activity. Appl. Sci. 8 (11), 2067. https://doi.org/10.3390/app8112067.

Moosavi, S., Lai, C.W., Gan, S., Zamiri, G., Akbarzadeh Pivehzhani, O., Johan, M.R., 2020. Application of efficient magnetic particles and activated carbon for dye removal from wastewater. ACS Omega 5 (33), 20684–20697. https://doi.org/10.1021/ACSOMEGA.0C01905/ASSET/IMAGES/LARGE/AO0C01905_0010.JPEG.

Pandi, K., Preeyanghaa, M., Vinesh, V., Madhavan, J., Neppolian, B., 2022. Complete photocatalytic degradation of tetracycline by carbon doped TiO2 supported with stable metal nitrate hydroxide. Environ. Res. 207,. https://doi.org/10.1016/J.ENVRES.2021.112188 112188.

Parmar, S., Daki, S., Bhattacharya, S., Shrivastav, A., 2022. Microorganism: an ecofriendly tool for waste management and environmental safety. Development in Wastewater Treatment Research and Processes 175–193. https://doi.org/10.1016/B978-0-323-85657-7.00001-8.

Pham, V.V., Truong, T.K., Hai, L.V., La, H.P.P., Nguyen, H.T., Lam, V.Q., Tong, H.D., Nguyen, T.Q., Sabbah, A., Chen, K.H., You, S. J., Cao, T.M., 2022. S-Scheme α-Fe2O3/g-C3N4Nanocomposites as Heterojunction Photocatalysts for Antibiotic Degradation. ACS Applied Nano Materials 5 (3), 4506–4514. https://doi.org/10.1021/ACSANM.2C00741/SUPPL_FILE/AN2C00741_SI_001.PDF.

Pirsaheb, M., Moradi, N., 2021. A systematic review of the sonophotocatalytic process for the decolorization of dyes in aqueous solution: Synergistic mechanisms, degradation pathways, and process optimization. J. Water Process Eng. 44,. https://doi.org/10.1016/J.JWPE.2021.102314 102314.

Preeyanghaa, M., Vinesh, V., Neppolian, B., 2022. Construction of S-scheme 1D/2D rod-like g-C3N4/V2O5 heterostructure with enhanced sonophotocatalytic degradation for Tetracycline antibiotics. Chemosphere 287,. https://doi.org/10.1016/J.CHEMOSPHERE.2021.132380 132380.

Ramutshatsha-Makhwedzha, D., & Nomngongo, P. N. 2022. Application of Ultrafiltration Membrane Technology for Removal of Dyes from Wastewater. 37–47. https://doi.org/10.1007/978-981-16-4823-6_3.

Samarghandi, M.R., Dargahi, A., Shabanloo, A., Nasab, H.Z., Vaziri, Y., Ansari, A., 2020. Electrochemical degradation of methylene blue dye using a graphite doped PbO2 anode: Optimization of operational parameters, degradation pathway and improving the biodegradability of textile wastewater. Arab. J. Chem. 13 (8), 6847–6864. https://doi.org/10.1016/J.ARABJC.2020.06.038.

Sharma, P.K., Cortes, M.A.L.R.M., Hamilton, J.W.J., Han, Y., Byrne, J.A., Nolan, M., 2019. Surface modification of TiO2 with copper clusters for band gap narrowing. Catal. Today 321–322, 9–17. https://doi.org/10.1016/J.CATTOD.2017.12.002.

Shi, Q., Ping, G., Wang, X., Xu, H., Li, J., Cui, J., Abroshan, H., Ding, H., Li, G., 2019. CuO/TiO2 heterojunction composites: an efficient photocatalyst for selective oxidation of methanol to methyl formate. J. Mater. Chem. A 7 (5), 2253–2260. https://doi.org/10.1039/C8TA09439J.

Silva, A.C.Q., Silvestre, A.J.D., Freire, C.S.R., Vilela, C., 2021. Modification of textiles for functional applications. Fundamentals of Natural Fibres and Textiles 303–365. https://doi.org/10.1016/B978-0-12-821483-1.00010-3.

Singh, M., Goyal, M., Devlal, K., 2018. Size and shape effects on the band gap of semiconductor compound nanomaterials. Journal of Taibah University for Science 12 (4), 470–475. https://doi.org/10.1080/16583655.2018.1473946.

Singha, K., Pandit, P., Maity, S., Sharma, S.R., 2021. Harmful environmental effects for textile chemical dyeing practice. Green Chemistry for Sustainable Textiles: Modern Design and Approaches 153–164. https://doi.org/10.1016/B978-0-323-85204-3.00005-1.

Tan, L., Xu, J., Zhang, X., Hang, Z., Jia, Y., Wang, S., 2015. Synthesis of g-C3N4/CeO2 nanocomposites with improved catalytic activity on the thermal decomposition of ammonium perchlorate. Appl. Surf. Sci. 356, 447–453. https://doi.org/10.1016/J.APSUSC.2015.08.078.

Thambiliyagodage, C., & Mirihana, S. 2021. Photocatalytic activity of Fe and Cu co-doped TiO2 nanoparticles under visible light. Journal of Sol-Gel Science and Technology 2021 99:1, 99(1), 109–121. https://doi.org/10.1007/S10971-021-05556-4.

Thambiliyagodage, C., Kumara, A., Jayanetti, M., Usgodaarachchi, L., Liyanaarachchi, H., Lansakara, B., 2022a. Fabrication of dual Z-scheme g-C3N4/Fe2TiO5/Fe2O3 ternary nanocomposite using natural ilmenite for efficient photocatalysis and photosterilization under visible light. Applied Surface Science Advances 12,. https://doi.org/10.1016/J.APSADV.2022.100337 100337.

Thambiliyagodage, C., Usgodaarachchi, L., 2021. Photocatalytic activity of N, Fe and Cu co-doped TiO2 nanoparticles under sunlight. Current Research in Green and Sustainable Chemistry 4,. https://doi.org/10.1016/J.CRGSC.2021.100186 100186.

Thambiliyagodage, C., Usgodaarachchi, L., Jayanetti, M., Liyanaarachchi, C., Kandanapitiye, M., Vigneswaran, S., 2022b. Efficient Visible-Light Photocatalysis and Antibacterial Activity of TiO2-Fe3C-Fe-Fe3O4/Graphitic Carbon Composites Fabricated by Catalytic Graphitization of Sucrose Using Natural Ilmenite. ACS Omega. https://doi.org/10.1021/ACSOMEGA.2C02336.

Tuyen, L.T.T., Quang, D.A., Tam Toan, T.T., Tung, T.Q., Hoa, T.T., Mau, T.X., Khieu, D.Q., 2018. Synthesis of CeO2/TiO2 nanotubes and heterogeneous photocatalytic degradation of methylene blue. J. Environ. Chem. Eng. 6 (5), 5999–6011. https://doi.org/10.1016/J.JECE.2018.09.022.

Van, K.N., Huu, H.T., Nguyen Thi, V.N., Le Thi, T.L., Truong, D.H., Truong, T.T., Dao, N.N., Vo, V., Tran, D.L., Vasseghian, Y., 2022. Facile construction of S-scheme SnO2/g-C3N4 photocatalyst for improved photoactivity. Chemosphere 289,. https://doi.org/10.1016/J.CHEMOSPHERE.2021.133120 133120.

Wu, Y., Chen, X., Cao, J., Zhu, Y., Yuan, W., Hu, Z., Ao, Z., Brudvig, G.W., Tian, F., Yu, J.C., Li, C., 2022. Photocatalytically recovering hydrogen energy from wastewater treatment using MoS2 @TiO2 with sulfur/oxygen dual-defect. Appl Catal B 303,. https://doi.org/10.1016/J.APCATB.2021.120878 120878.

Wu, Z., Yuan, D., Lin, S., Guo, W., Zhan, D., Sun, L., Lin, C., 2020. Enhanced photoelectrocatalytic activity of Bi2S3–TiO2 nanotube arrays hetero-structure under visible light irradiation. Int. J. Hydrogen Energy 45 (56), 32012–32021. https://doi.org/10.1016/J.IJHYDENE.2020.08.258.

Yang, J., Liu, Z., Wang, Y., Tang, X., 2020. Construction of a rod-like Bi2O4 modified porous g-C3N4 nanosheets heterojunction photocatalyst for the degradation of tetracycline. New J. Chem. 44 (23), 9725–9735. https://doi.org/10.1039/D0NJ01922D.

Yang, M., Qian, Y., Du, J., Yuan, S., Wang, S., Zhu, X., Lin, X., Li, K., Li, S., Kang, D.J., 2018. Controlled synthesis of nanoplate, nanoprism and nanopyramid-shaped CdSe decorated on porous TiO2 photocatalysts for visible-light-driven hydrogen evolution. Ceram. Int. 44 (11), 12555–12563. https://doi.org/10.1016/J.CERAMINT.2018.04.052.

Yu, X., Liu, Z., Wang, Y., Luo, H., Tang, X., 2020. Fabrication of corncob-derived biomass charcoal decorated g-C3N4 photocatalysts for removing 2-mercaptobenzothiazole. New J. Chem. 44 (37), 15908–15918. https://doi.org/10.1039/D0NJ04057F.

Yu, X., Liu, Z., Zhu, Z., Luo, H., 2023. Controllable construction 2D-CN photocatalyst for degradation MBT and mechanism insights. Mater. Res. Bull. 159,. https://doi.org/10.1016/J.MATERRESBULL.2022.112093 112093.

Zhu, Z., Kumar, R., Luo, L., Varjani, S., Huo, P., Wong, J.W.C., Zhao, J., 2022. Quantum effect and Mo–N surface bonding states of α-MoC1−x modified carbon nitride for boosting photocatalytic performance. Cat. Sci. Technol. 12 (21), 6384–6397. https://doi.org/10.1039/D2CY01157C.